Proceedings of ASME Turbo Expo 2011
GT2011
June 6-10, 2011, Vancouver, British Columbia, Canada

GT2011-45214

EFFECTS OF ROTATING STALL ON AN AXIAL FAN DESIGN

K.R. Wilt
Department of Mechanical,
Aerospace and Nuclear Engineering
Rensselaer Polytechnic Institute
Troy, NY, 12180

D. Story
General Electric Company
Schenectady, NY 12345

H.A. Scarton
Department of Mechanical,
Aerospace and Nuclear Engineering
Rensselaer Polytechnic Institute
Troy, NY 12180

A.I.C. Hunter
Atlas Copco
Voorheesville, NY 12186

S.A. Salamah
General Electric Company
Schenectady, NY 12345

J. Ramtahal
General Electric Company
Schenectady, NY 12345

ABSTRACT

This paper presents the physical measurements and analysis of data pertaining to rotating stall observed during testing at the GE fan test facility located at Rensselaer Polytechnic Institute. Although never detected in actual GE applications, the rotating stall was encountered while testing fan cooling blade prototypes used in electrical generators. The effects of this phenomenon on the flow rate and pressure rise across the fan are considered, along with the frequency content of the adjacent flows on either side of the fan. Further, the effects of the addition of flow constrictions before and after the fan on the behavior of the rotating stall are investigated.

INTRODUCTION

The GE fan test facility, located at Rensselaer Polytechnic Institute has been in operation to verify the performance characteristics of axial flow ventilation fans designed with CFD tools. For some of the blade profiles tested, rotational stall was evident when higher system impedances, or flow resistances, were enforced. This rotational stall resulted in significantly reduced fan flow rates and pressure rises as compared to when the fan was not experiencing rotating stall.

Rotating stall is an operating condition in which flow separation around a blade profile is evident and may occur in any type of turbo-machine [1]. In most cases, this separation zone will grow and cascade to the next passing blade. This growth builds a ”cell” of disturbance. The cell will rotate around the rotor at a fraction of the operational speed and its effects will propagate both up and downstream of the fan. The rotation of the cell at a fraction of the operational speed implies that once the cell is generated, the blade that produced the cell will eventually leave the disturbance, in effect returning to a state of attached flow. The blade will encounter the same stall cell, or another cell should there be multiple, with further rotation of the fan.

It has been shown that the number of stall cells may be related to the amount of flow resistance in the flow path. As described by Sorokes [1] and also by Poesngen et al. [2], as the flow resistance is increased, which effectively reduces the flow rate, the number of stall cells evident increased as well. A summary of means to determine the number and speed of the cells is presented in [3].

Since the rotation of the stall cells is slower than the actual fan, the low frequency noise emissions will in turn increase. This effect further demands that the rotating stall phenomenon be understood and accounted for during design to ensure proper operation of the fan and to also limit the acoustic pollution.

Numerous experimental observations have been published on rotating stall [4–9]. These works include results from both

axial and centrifugal compressor/fan designs. Some empirical models derived from observations of axial compressors are given by Greitzer [10]; and from centrifugal compressors by Frigne and Braembussche [11]. Speziale et al. [12] studied the propagation of stall in linear blade cascades using vortex methods. Numerical studies of rotating stall have also been published by several authors [13–15]. Day [16] has investigated the use of individually controllable air injection valves (upstream of the compressor) as a means of active suppression of both stall and surge for an axial compressor. On the topic of the inception of rotating stall, several works have been published [17–20] in an effort to increase understanding the reasons behind it.

Most of the previous experimental work done on the topic of rotating stall was with compressors and not fans. This paper presents measurements of the rotating stall from three fans designs and describes the effects of rotating stall on the flow rate and other system characteristics.

FAN TEST FACILITY

The fan test facility is located in the Laboratory for Noise and Vibration Control Research at Rensselaer Polytechnic Institute. The rig was initially designed as an approximate three-quarter scale (0.73) model of the ventilation fan for a 51H generator, shown in Figure 1, but has since been used to test fan blades from multiple generator types.

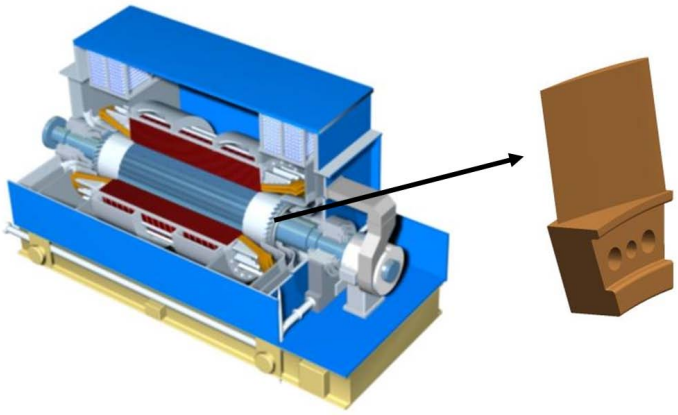

FIGURE 1. Software representation of 51H generator

The fan test rig was designed to conform to specifications described within the ANSI/AMCA standard "Laboratory Methods of Testing Fans for Aerodynamic Performance Rating" [21]. The standard describes multiple test configurations with pressure and temperature measurement location requirements from which the RPI fan test facility was based.

Shown in Figure 2 is a schematic of the fan test rig's physical configuration with the location of the sensing planes for each pressure measurement taken during an experiment. The drawing is essentially a vertical cross-section of the test chamber, where the cross-section plane is coincident with the rotational axis of the fan. Further, the drawing is roughly to scale, with the chamber's height dimension being reduced to allow for a simpler representation. The flow path for the test rig starts at the extremities of the inlet plenum. This inlet plenum is a rectangular space with the top and bottom of the construction open. The flow travels radially towards the axis of the fan and is redirected to flow axially with the fan via inner and outer flow guides (the inner flow guide is the guide that surrounds the fan while the outer guide is the one preceding the fan in the flow path). After passing through the fan, the flow is allowed into a large chamber, which is approximately 1.2 meters wide and 2.4 meters long and tall (4x8x8 feet). The fan is centered horizontally to the chamber inlet face but not vertically. The dimension from the base of the chamber to the fan axis is 0.91 m (3 ft). The flow exits the chamber via a 0.38 m (15 in) diameter outlet nozzle which is coaxially aligned with the fan.

Directly in the middle of the chamber is a means to add flow impedance. The flow impedance is implemented by cloth inserts composed of either a thick felt or a thin muslin fabric wrapped around a reinforcing wire mesh. Using different combinations of felt and muslin inserts (typically referred to simply as 'felt'), a variety of system impedances could be produced. Figure 3 presents a photo, taken from the viewpoint of the outlet nozzle, of the muslin fabric insert added to the flow path. In addition to the felts, wooden constrictors were added to the rig's inlet plenum openings in some tests to reduce the available flow cross-section, causing significantly increased system impedances.

Measurements of the static gauge pressures were done inside of the inlet plenum and within the chamber (upstream of the felt inserts). Four individual measurements of the differential pressure (ΔP) across the fan and a single differential pressure measurement across the outlet nozzle were done. Excluding the four individual fan ΔP measurements, the pressure measurements at each of the sensing planes consisted of four taps (two for the inlet plenum plane) physically averaged by linking the taps together via tubing. The taps themselves were 1 mm (0.04 in) in diameter on the tap face, whereas the tubing used was 6.35 mm (0.25 in) in diameter. A pitot tube was also mounted within the outlet nozzle's throat to measure the total and static pressure of the flow at various transverse locations. Measurement of the temperature of the flow at each of the pressure measurement planes was also done via RTD probes.

Since the publication of [22], the inlet of the test facility has been redesigned such that the differential pressure taps across the fan blades have a more standardized location while also increasing the structural stability of the rig. The new inlet configuration, which is reflected in Figure 2, allows the fan to operate

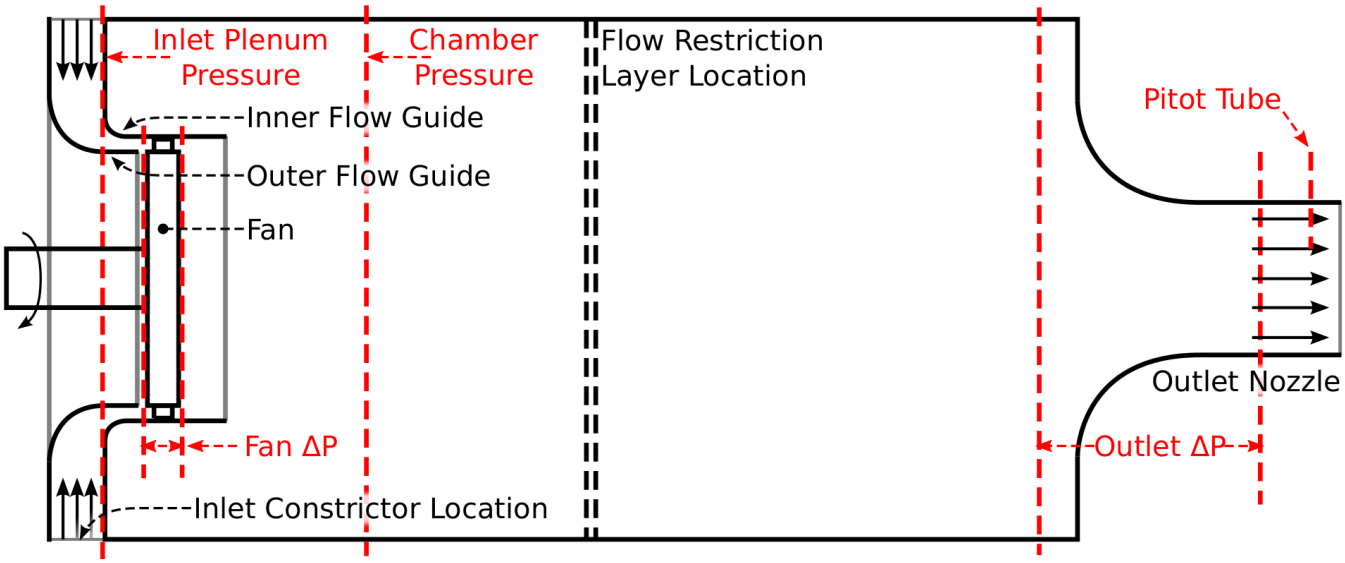

FIGURE 2. Schematic of the fan test rig's flow path with sensor planes marked.

in a cylindrical-flow region, reducing the effects of flow turning on the upstream pressure tap. This configuration supports both an 11-bladed and 22-bladed fan configuration, with an 11-bladed fan's axial thickness being roughly twice as large as a 22-bladed fan's axial thickness. To support this change in thickness, two sets of static pressure taps are present on the upstream side (low pressure) of the differential pressure measurement across the fan. The set of upstream pressure taps designed to accommodate the 11-bladed fan are 122 mm (4.8 in) upstream of the high-side pressure taps whereas the distance for the 22-bladed fan configuration is only 76 mm (3.0 in). These dimensions were selected to allow the pressure taps to be approximately 13 mm (0.5 in) upstream and downstream of the blade tip and tail, respectively. Each set of taps used in the fan ΔP measurement was composed of four individual taps spaced circumferentially equidistant around the inner flow guide. The values of the fan ΔP found in this report are the average of each of the four individual differential measurements.

In addition to the static pressure taps, there was also three dynamic pressure sensors mounted within the inner flow guide. One of these sensors was located in plane with the static pressure taps upstream of the fan (note that this plane is perpendicular to the fan axis and is marked in Figure 2) while the other two were placed in line with the downstream taps. One of the downstream dynamic pressure sensors was circumferentially aligned with the upstream sensor, while the other downstream transducer was mounted 90° from the other two in the direction of the fan's rotation. In Figure 4, the trailing edge of the fan is shown, along with the downstream side of the fan differential pressure probe location (circular white plastic insert) and a dynamic pressure sensor mounted within a circular brass insert, with the sensing face of the transducer tangent with the inner flow guide.

The flow rate produced by the fan was calculated via the outlet nozzle's ΔP measurement taken across taps just upstream of the outlet nozzle, and within the nozzle's throat. Using the previously mentioned pitot tube, a nozzle calibration routine was completed to associate the outlet ΔP to the flow rate [21].

The fan was spun by a 56 kW (75 hp) electric motor via a 3:1 belt drive. A 60-tooth magnetic pickoff tachometer was mounted on the fan's shaft for monitoring of the fan speed. This sensor was also used as feedback in the speed control (control was generated by a PC running National Instruments' LabVIEW).

All sensor data was captured via a data acquisition program created using LabVIEW. For all the sensors, excluding the dynamic pressure sensors and tachometer, a set of readings (250 points at 1000 kHz) was acquired, averaged, and recorded once a second during a test. The static pressure transducers were Omega Engineerings PX-655 differential pressure transducers, where non-differential measurements had the low (or high) side pressure tap open to the atmosphere. Twenty readings of the tachometer were taken and averaged every second, while the dynamic pressure transducers (Endevco 8510B-2 piezoresistive transducer, bidirectional 13.8 kPa (2 psi) range with 0.02% non-repeatability) was sampled at 51.2 kHz (with anti-aliasing filters ensuring alias free data up to 23 kHz), typically over a 10-second span.

TEST CASES

Three different fan geometries are presented in this work. Two 11-bladed fans were tested whose blade profiles were of a General Electric proprietary design. Unfortunately, due to the

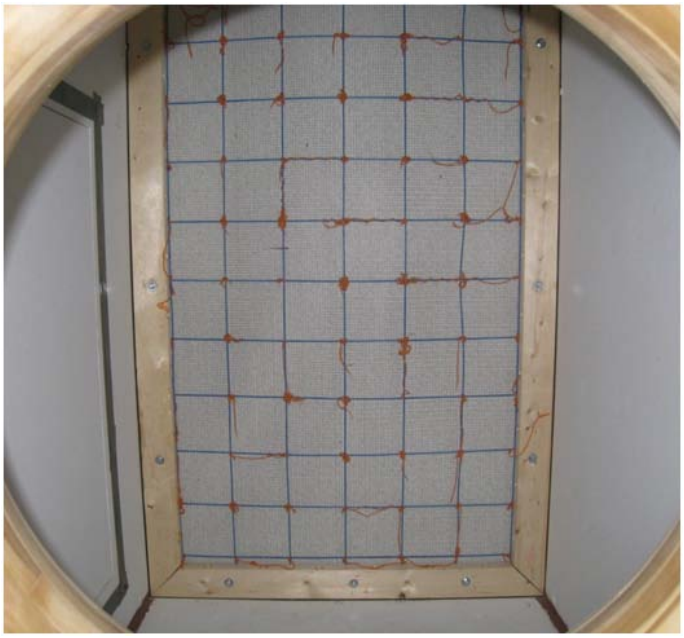

FIGURE 3. Photo of cloth insert layer within the flow path. Photo is taken from the outlet nozzle towards the fan (not visible).

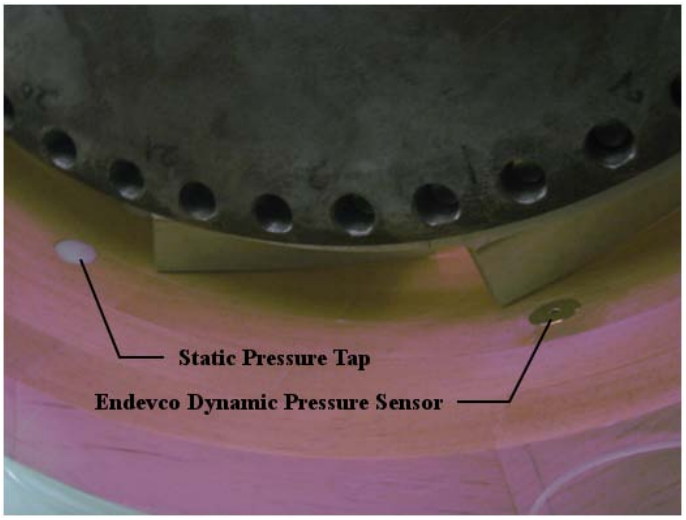

FIGURE 4. Photo of trailing edge of fan within inner flow guide

profile designs being proprietary, the geometry of the blades are not presented in this paper other than the fact that one of the geometries had an angle of attack of 20° and the other had an angle of attack of 30°. The target operating speed of both these geometries was 1730 rpm.

The third geometry presented is a 22-bladed fan whose blade shape was a NACA 65-410 profile with an angle of attack of 20.5°. Due to the 22-bladed fan having a different end application as compared to the 11-bladed fan, the desired operating speed for this fan was 4109 rpm.

For each of the fan geometries presented in this paper, the blade height was 38.1 mm (1.5 in), the outer diameter of the fan was 711.2 mm (28 in) and the average blade tip clearance was 1.6 mm (0.063 in) from the inner flow guide.

Testing of each of the fan geometries was done by running the fan at the desired speed with various system impedances and holding at the desired speed for at least 30 seconds. The recorded data for the static measurement probes was averaged over this measurement time. A final test was also done where the outlet nozzle was completely obstructed, resulting in a no-flow operating condition. By plotting each of the tests done for a single fan over the various system impedances, a characteristic curve was generated.

FAN PERFORMANCE RESULTS

Using the system impedance modifications mentioned previously, the characteristic curve for each of the test case profiles was produced and are presented in Figures 5, 6, and 7, where the test points which were identified to have been operating in a rotating stall condition are labeled. For each of the marked stall points, the determination of the presence of rotating stall was confirmed via dynamic pressure analyses (see following section), except for the marked point in Figure 5, where the dynamic transducer had yet to be installed. For each fan blade profile, it was fairly obvious that the rotating stall had a significant effect on the fan pressure rise and flow rate. For both the 20° and 65-410 blades, only one stall point was evident at the testing speed while the 30° blades had nearly half the test points in stall.

In Figures 5-7, the horizontal axis normalization to percentages was done by dividing the flow rates for each individual test by the maximum flow rate measured during testing, hence the highest flow rate in the measurements group for each case was located at 100%. The vertical axis was normalized to the fan pressure rise evident during the no-flow test for each of the fan geometries. Note that normalization via the no-flow condition results in the no-flow test point being located at 0% flow rate and 100% fan pressure rise for each figure; and hence, the points are not shown in any of the figures.

Also shown in these figures are analytical results obtained from CFD (Computation Fluid Dynamics) models of each of the fans. The CFD method used to compute these results is the same that was described in [22]. The models of the fan consisted of a single blade with periodic boundary conditions. Due to this, prediction of a rotating stall condition is not possible. The model does however predict a pure stall condition (where all blades are in stall). This pure stall condition is what causes the analytical results to peak (in terms of the fan ΔP) and begin to decrease as the flow rate decreases. The ΔP peak for each case was predicted to have a similar magnitude as compared to the measurements,

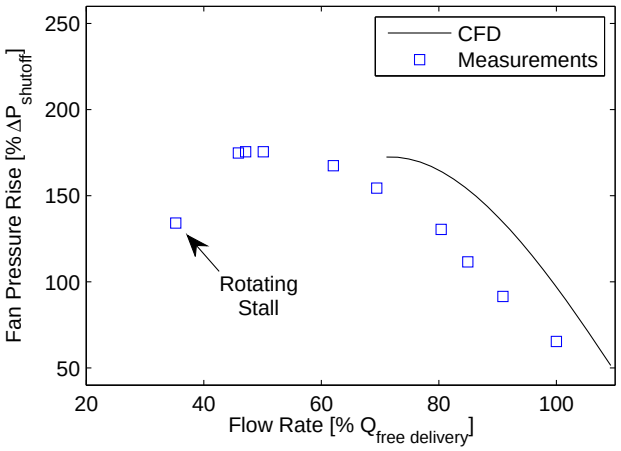

FIGURE 5. Characteristic curve for 20° 11-bladed fan at 1730 rpm

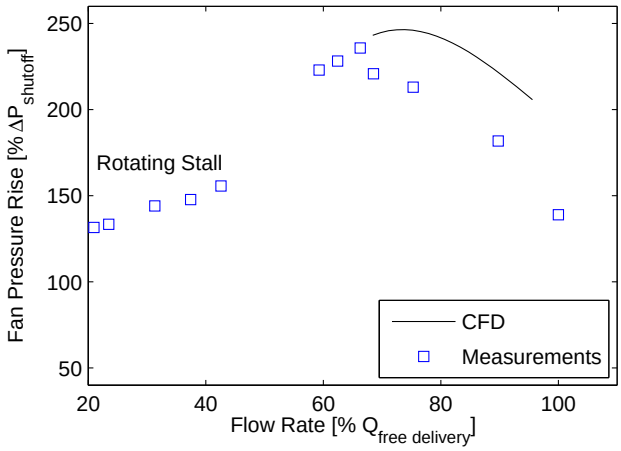

FIGURE 6. Characteristic curve for 30° 11-bladed fan at 1730 rpm

while the peak was calculated to occur at a flow rate which was much higher than the actual measurements exhibit. Further, the slope of the fan ΔP vs. flow rate when rotating stall was not apparent matched well between the CFD results and test measurements. The discrepancies between the measurements and simulation may arise from the model being unable to simulate asymmetric conditions which are evident in the actual test rig (e.g., the inlet plenum being rectangular with inlets only on the top and bottom) and also that the CFD model was meant to represent operation of the fan blade while attached to a generator's rotor (an extended length) while the test rig's rotor has only a 76 m (3 in) axial length.

ANALYSIS OF ENCOUNTERED ROTATING STALL

The distinction between regular operation and the rotating stall condition was done via analysis of the time and/or frequency domain data taken from the dynamic pressure transducers mounted near the fan. It is shown in this section that for the dynamic pressure measurements there was very little excitation of frequencies lower than that of the blade passing frequency whereas during a stall condition, there was a low frequency pressure pulsation. From this pressure pulsation, it was possible to determine how fast the stall cell(s) were rotating and the number of cells. Fan surge was not found to be the cause of the low frequency pressure pulsation as surge is characterized by an axisymmetric pulsation [4], which was not evident in any of the analyzed data.

For reference, as stated before, the dynamic data was sampled at 51.2 kHz for 10 seconds. This implies a frequency domain analysis has a 0.1 Hz resolution. For the analysis presented, the data was windowed via a Hanning window. Conversions from time to frequency domain were done via an FFT.

Shown in Figure 8 is data taken from the upstream dynamic

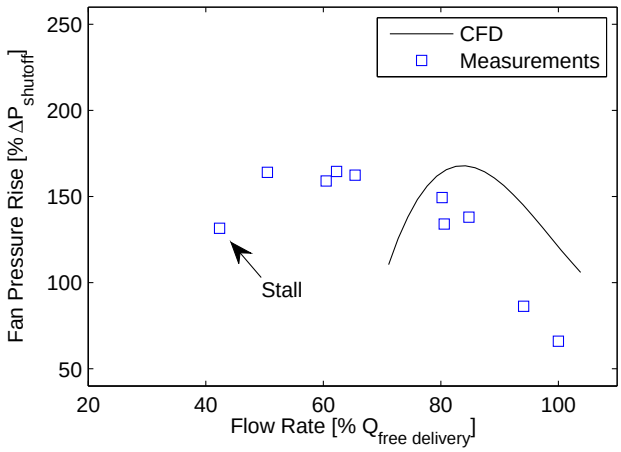

FIGURE 7. Characteristic curve for 20.5° NACA 65-410 22-bladed fan at 4109 rpm

pressure transducer for the 11-bladed 30° geometry for both the stall and no-stall conditions where the fan speed was specified as 1200 rpm (this data and operating speed were selected as they represent a case where the fan was run in both a stall and no-stall condition as discussed in the following section). Two frequency peaks are marked on the no-stall condition in the given frequency range: 20 Hz, which corresponds to the fan speed (1200 rpm = 20 Hz), and 40 Hz, the running speed's second harmonic. Two new frequency peaks manifest at 10.5 and 20.9 Hz during stall, with the 20.9 Hz peak enveloping the 20 Hz running speed peak. The peak at 10.5 Hz (∼50% running speed) corresponds to the pressure pulsation caused by the stall cell(s), whereas the 20.9 Hz appears to be a harmonic of the 10.5 Hz signature. The difference between these two operational cases in the time domain as measured by the upstream sensor is shown in Figure 9, where the pressure induced by the passing of the blades by the sensor is

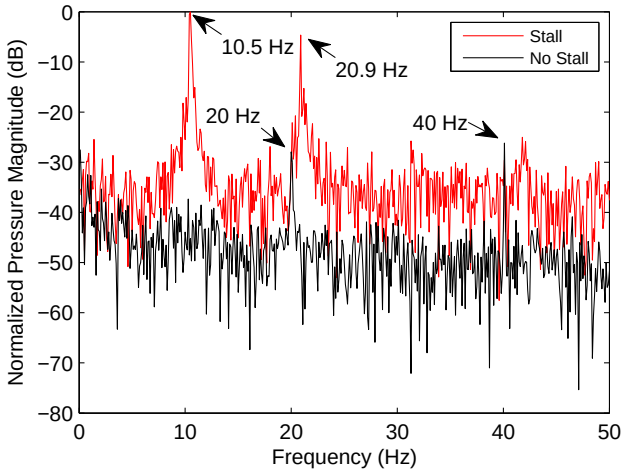

FIGURE 8. Frequency domain comparison (FFT) of stall and no-stall conditions for 30° 11-bladed fan geometry running at 1200 rpm. The y-axis was normalized to the maximum peak in decibels.

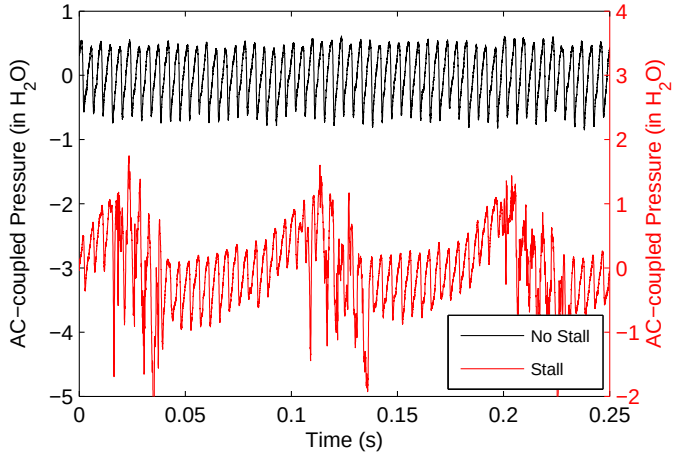

FIGURE 9. Time domain comparison of upstream pressure responses during stall and no-stall conditions for 30° 11-bladed fan geometry running at 1200 rpm

obvious for each case and the rotating stall low-frequency signature obvious for its respective case.

The number of stall cells present can be determined by looking at the phase difference of the stall frequency signature between the two in-plane downstream dynamic pressure transducers. Since the two downstream sensors are known to be 90° apart circumferentially, the number of stall cells may be deduced by looking at the phase difference of the two responses at the stall signature's frequency peak (either computed via subtraction of the two phases or computed via a cross-spectrum analysis). If it is assumed that the stall cell(s) rotate with the rotor but at a fraction of the speed, the number of cells may be determined by:

$$n_{cells} = \frac{\Delta\theta}{90^\circ} + 4k \tag{1}$$

where $\Delta\theta$ is the phase difference between the two sensor readings, which is positive and rounded to the nearest 90° multiple, and k is a positive integer. Rounding of the phase difference to the nearest 90° multiple is required due to the design of the fan test rig not being axisymmetric. The asymmetries may lead to the stall cell's rotational velocity being variable with respect to the circumferential position of the cell, which in turn would cause the calculated phase differences between the pressure transducers to stray from the 90° increments. Note that this equation allows for the possibility of a theoretical infinite number of stalls cells for each phase difference value thanks to the integer k, where in actuality the maximum amount of stall cells possible is a fraction of the number of blades considering that stall cells may grow to engulf multiple blades at once. In light of this, it is presumed to be unlikely that any rotating stall operating condition encountered may have had any more than 4 stall cells; therefore, it is assumed here that k is equal to 1.

Knowing the number of active cells makes it possible for the calculation of the rotational speed of the cell(s) around the fan. The rotational speed is calculated by taking the frequency at which the number of cells was found and dividing it by said number of cells.

For the case shown in Figure 8, the phase difference of the two dynamic pressure transducers downstream was calculated to be -278°, or equivalently, 82°, via a cross-spectrum analysis. This implied that the system had only one stall cell rotating around the shaft axis at 10.5 Hz.

A graphical method to accomplish the same result is described in [3]. In Figure 10, this method is applied to the data used above for the 30° 11-bladed fan running at 1200 rpm case. By drawing a line through similar points in the pressure variation time signal for each sensor signal, where the signals are plotted with respect to their circumferential alignment (with the sensor at 0° repeated at 360°), it is determined that T_{CR} (or the cell rotation period, which is measured via the horizontal length of the dashed red lines) is approximately 0.1 s; reinforcing the previous conclusion that the stall cell was rotating at 10.5 Hz. Further, since T_{CR} was equal to T_{OSC} (the pressure oscillation period), the number of stall cells is deduced to be 1 via the equation [3]:

$$n_{cells} = \frac{T_{CR}}{T_{OSC}} \tag{2}$$

Another rotating stall case for the same blade set was analyzed while operating at the target speed (1730 rpm) with the

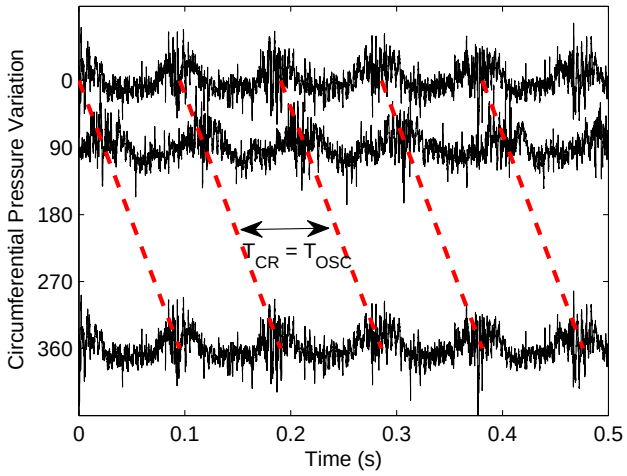

FIGURE 10. Pressure variation of downstream flow with respect to transducer locations. Data is from 30° 11-bladed fan running at 1200 rpm

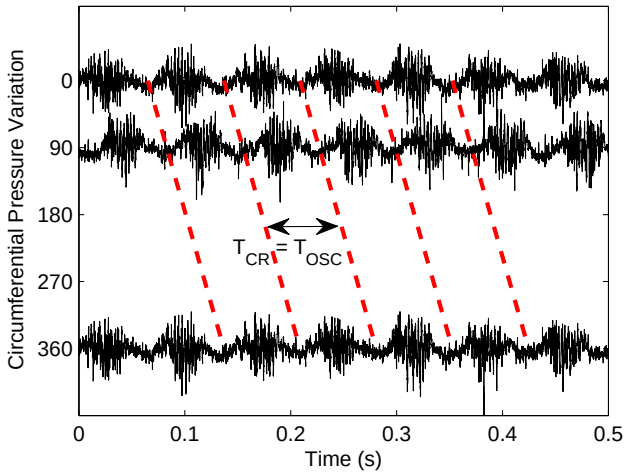

FIGURE 12. Pressure variation of downstream flow with respect to transducer locations. Data is from 30° 11-bladed fan running at 1730 rpm

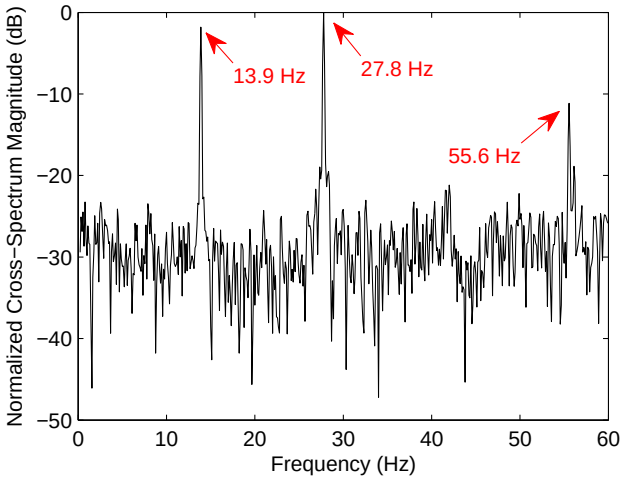

FIGURE 11. Magnitude of the cross-spectrum between the two downstream dynamic pressure sensors for the 30° 11-bladed fan geometry running at 1730 rpm

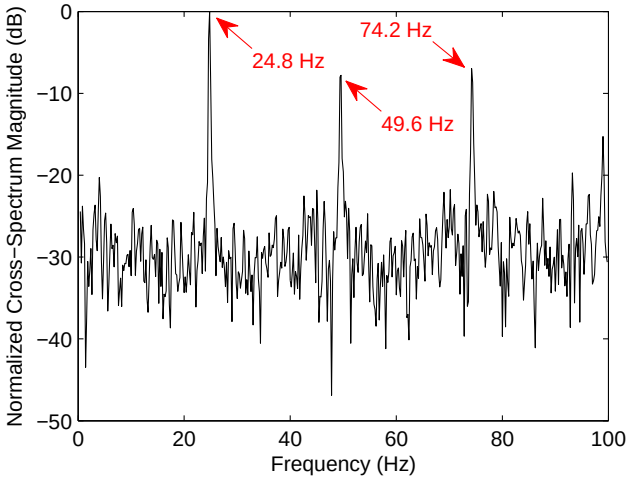

FIGURE 13. Magnitude of the cross-spectrum between the two downstream dynamic pressure sensors for the 22-bladed 20.5° NACA 65-410 fan geometry running at 4109 rpm

maximum available system resistance. Note that this case is the test point in Figure 6 with the least amount of flow. The cross-spectrum between the two downstream transducers for this test is shown in Figure 11. An interesting note in this case is that the first rotating stall signature peak (at 13.9 Hz, or 48% running speed) is of a slightly lower magnitude as compared to the second peak at 27.8 Hz (96% running speed). Due to this, it is slightly ambiguous as to the number of stall cells evident. On one hand, if the 13.9 Hz is assumed to be the main signature, the phase reported at that peak points towards 1 stall cell (94.5°) whereas if the 27.8 Hz peak is assumed to be the main signature, 2 stall cells are evident (phase of 169.6°). Interestingly, the calculated rotational speed of the stall cells will be 13.9 Hz regardless of the chosen peak.

In an effort to reduce the ambiguity on the number of stall cells, the time domain pressure variation is plotted in Figure 12. From this figure, it seems fairly clear that there is only one stall cell rotating at 13.9 Hz.

The same test was conducted at 4109 rpm with the maximum system resistance available (without stopping flow completely) for the 22-bladed 20.5° NACA 65-410 geometry. Note that this is the only point in Figure 7 in which the fan was expe-

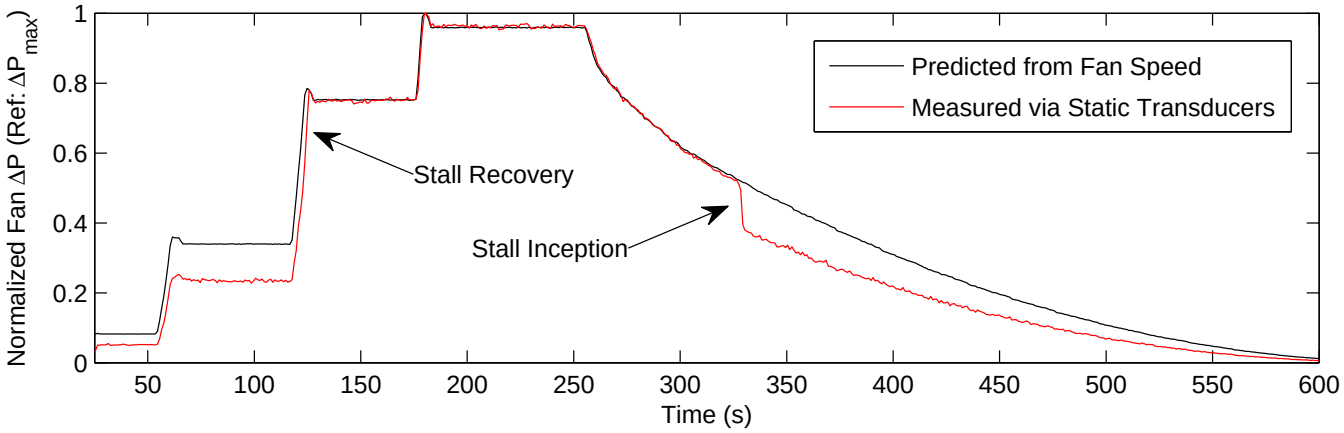

FIGURE 14. Comparison of the predicted normalized fan pressure rise from the fan speed and the actual measured normalized fan pressure rise for the 20° 11-bladed fan with two felt insert layers in flow path. Note that the fan speed was held at three different speeds: 1000, 1500 and 1730 rpm

riencing rotating stall. The cross-spectrum magnitude of the two downstream transducers is shown in Figure 13. The phase of the cross-spectrum at the 24.8 Hz peak, 64.1°, indicated that, again, a single stall cell was apparent and was rotating at 36% of the fan speed.

From the test data analysis shown here and others which were not, it seems that only one stall cell was ever encountered during the fan's operation.

BEHAVIOR OF ROTATING STALL WITH RESPECT TO FAN SPEED

At lower operational speeds, the rotating stall phenomenon was more frequent than as shown in Figures 5-7. When any of the given fan configurations were turned on and accelerated, it was typical to see a stall-to-no-stall transition at some point during the ramp up, which was done at 80 rpm/s. To illustrate this, Figure 14 is presented, which shows the predicted value of the normalized fan ΔP derived from the fan speed ($Speed^2/Speed^2_{max}$) compared to the measured value ($Measured/Measured_{max}$). The "$Measured_{max}$" value used to normalize the fan ΔP in this case occurred when the system was not experiencing stall and as a result, the predicted values of the fan ΔP via the speed relate to this no-stall condition. As such, it is obvious that the prediction fails at all times prior to approximately 125 s and after 325 s. This is a result of the system starting within the stall condition (0-125 s), then leaving the rotating stall regime (125-325 s) and finally slipping back into stall (325-600 s). Similar results have been observed (i.e. the drop in fan pressure rise while decelerating) for both of the other test cases; however, the sudden drop in fan pressure rise (the slip back into rotating stall) typically did not occur until a significantly lower fan speed, and hence, significantly lower fan ΔPs.

In Figure 14, it must be highlighted that the stall-to-no-stall (stall recovery) and no-stall-to-stall (stall inception) transitions did not occur at the same fan pressure rise, with the latter taking place at a lower pressure rise than compared to the former (a hysteresis effect). This effect is illustrated in Figure 15 via plotting of the normalized pressure rise (again calculated by $Measured/Measured_{max}$) with respect to the fan speed (note that Figure 15 uses the same test data as used in Figure 14). In Figure 15, it is also shown that the fan pressure rise in both operational regions follow a parabolic trend with respect to the fan speed. This implies that fan scaling laws are applicable even when the fan is in a stall condition. However, using fan scaling laws to move a stall condition to a higher fan speed or flow rate may be troublesome as the scaling does not account for the possibility of the fan leaving the rotating stall regime.

The hysteresis effect was also apparent in the flow rate response of the system, as shown in Figure 16. The spread of the data in Figure 16 at lower speeds/flow rates may be attributed mainly to quantization error and the measurement being less than 3% of the pressure transducer's range and therefore should be ignored (the data is still presented for trend visualization purposes). As reference, the stated accuracy of the transducer used to measure the flow rate calculates to be approximately 0.2 on the normalized flow rate axis. Since flow rate increases proportionally to the square root of the pressure drop, the accuracy of the flow rate measurement increases quickly over the given span.

Considering the hysteresis effect shown in the fan pressure rise and flow rate responses, it is possible for the fan to operate at ranges of operational speeds, fan pressure rises and flow rates at which both the stall and no-stall conditions may be possible. This allows for the direct comparison of the stall and no-stall conditions where no other physical properties of the rig have been modified. For the 11-bladed 30° profile geometry, a stall and no-stall condition was found and tested at a constant fan speed (1200 rpm). The results of this test revealed an approximate decrease

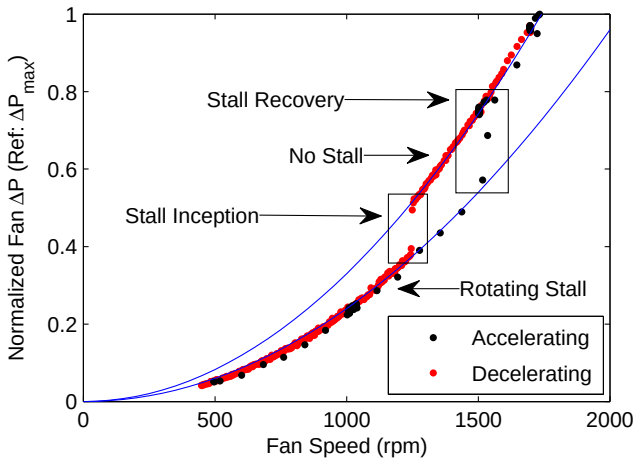

FIGURE 15. Normalized fan ΔP vs. fan speed for 20° blades

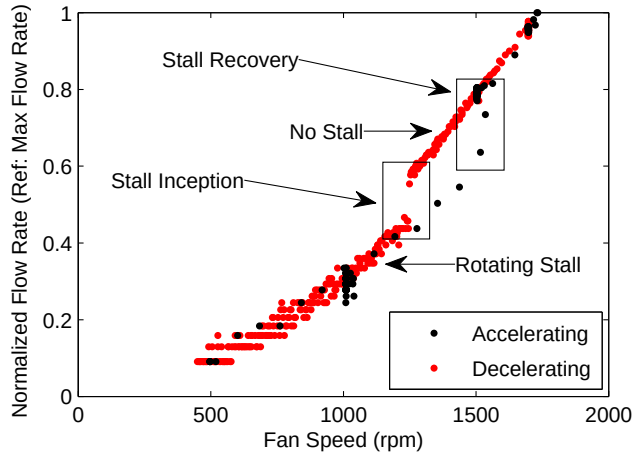

FIGURE 16. Normalized flow rate vs. fan speed for 20° blades

of 1/5-1/3 for certain system parameters when going from the no-stall condition to stall. The relative magnitude difference of some of the system performance parameters in the stall condition as compared to the no-stall condition are presented in Table 1. Note that the data used to create this table was obtained from the same test which produced the data in Figures 8 and 9.

It would have been preferable to reproduce Table 1 with data from either of the other two configurations, but unfortunately the data required to do this is not available. Similar drops in system parameters are expected however as the production of plots akin to Figure 15 for many different configurations (including for the three tested profiles) resulted in a comparable difference between the rotating stall and regular flow fit curves (shown both as blue lines in Figure 15) each time. For instance, the relative magnitude of the fan pressure rise curve fits for the 30° 11-bladed fan with the largest available system impedance that allows for no-stall operation at 1730 rpm was calculated to be 71% (Note that this test is not the same as presented in Table 1). For the 65-410 blades, again with the largest available system impedance that allows for no-stall operation at 4109, the relative magnitudes of the parabolic curves was calculated to be 79%. The relative difference of the fits shown in Figure 15 (20° blades) is 73%.

TABLE 1. Relative magnitude of select system parameter values when in stall compared to the no-stall condition for 30° blades at 1200 rpm

Drive Power	Fan Pressure Rise	Flow Rate
81%	74%	79%

Inlet Plenum Pressure	Chamber Pressure
64%	71%

CONCLUSIONS

In this work, instability in the fan's operation was observed and evidence of the rotating stall behavior was presented. The behavior was found to be evident mainly at large system resistances, but could also happen at lower resistances depending on the blade geometry. Further, it was found that for most cases the fan started operation in a rotating stall mode but as the fan was accelerated, the system recovered and the rotating stall vanished. Whenever this happened, the stall regime was most likely re-entered during deceleration of the fan, but at a lower fan pressure rise and flow rate as compared to the initial stall recovery transition (a hysteresis effect). This made it possible for an operating speed to run in both the stall and no-stall conditions, depending on the running history. Using the hysteresis characteristic of rotating stall, it was possible to directly determine the effects that the rotating stall has on the certain system characteristics, e.g., flow rate and fan pressure rise. It was found that the appearance of rotating stall could be expected to reduce system performance parameters to ∼65-80% of the performance of the fan if stall was not present. Finally, it was also shown that even though the system dynamics had changed significantly within the rotating stall operation mode, fan scaling laws were still applicable.

The dynamic data presented showed that when the maximum system resistance was implemented, the 30° 11-bladed fan and the 20.5° NACA 65-410 22-bladed fan both experienced rotating stall with only 1 stall cell (no data was obtained for the 20° 11-bladed fan). It is known to be possible that multiple stall cells may be present at even higher system impedances [1,2], but testing for these cases was not possible with the current rig configuration. Considering that only 1 stall cell was encountered, the conclusions made about the reduction in performance due to rotational stall may only be applicable to the 1 stall cell case.

NOMENCLATURE

$NACA$	National Advisory Committee for Aeronautics
CFD	Computational Fluid Dynamics
P	Gauge Pressure
ΔP	Differential Pressure
Q	Volumetric Flow Rate
T_{CR}	Cell Rotation Period
T_{OSC}	Pressure Oscillation Period
$\Delta\theta$	Phase Difference
n_{cells}	Number of Stall Cells

ACKNOWLEDGEMENTS

This work was sponsored by the GE Generator Engineering.

REFERENCES

[1] Sorokes, J., 2003. Rotating stall - an overview of dresser-rand experience. Tech. rep., Dresser-Rand.

[2] Poensgen, C., and Gallus, H., 1996. "Rotating stall in a single-stage axial flow compressor". Journal of Turbomachinery, **118**(2), pp. 189–196.

[3] Levy, Y., and Pismenny, J., 2003. "The number and speed of stall cells during rotating stall". In Proceedings of the ASME 2003 Turbo Expo, pp. 889–899.

[4] Greitzer, E., 1976. "Surge and rotating stall in axial flow compressors - part i: Theoretical compression system model". Journal of Engineering for Power, **98**, pp. 190–198.

[5] Frigne, P., and Braembussche, R. V. D., 1984. "Distinction between different types of impeller and diffuser rotating stall in a centrifugal compressor with vaneless diffuser". Journal of Engineering for Gas Turbines and Power, **106**(2), pp. 468–474.

[6] Kinoshita, Y., and Senoo, Y., 1985. "Rotating stall induced in vaneless diffusers of very low specific speed centrifugal blowers". Journal of Engineering for Gas Turbines and Power, **107**(2), pp. 514–519.

[7] Cellai, A., Ferrara, G., Ferrari, L., Mengoni, C., and Baldassarre, L., 2003. "Experimental investigation and characterization of the rotating stall in a high pressure centrifugal compressor: Part iii - influence of diffuser geometry on stall inception and performance (2nd impeller tested)". pp. 711–719.

[8] Carnevale, E., Ferrara, G., Ferrari, L., and Baldassarre, L., 2006. "Experimental characterization of vaneless diffuser rotating stall: Part v - influence of diffuser geometry on stall inception and performance (3rd impeller tested)". In Proceedings of the ASME 2006 Turbo Expo, pp. 1095–1103.

[9] Sano, T., Nakamura, Y., Yoshida, Y., and Tsujimoto, Y., 2002. "Alternate blade stall and rotating stall in a vaned diffuser". International Journal Series B Fluids and Thermal Engineering, **45**(4), pp. 810–819.

[10] Greitzer, E., 1976. "Surge and rotating stall in axial flow compressors, part ii: Experimental results and comparison with theory". Journal of Engineering for Power, **98**, pp. 199–217.

[11] Frigne, P., and Braembussche, R. V. D., 1985. "A theoretical model for rotating stall in the vaneless diffuser of a centrifugal compressor". Journal of Engineering for Gas Turbines and Power, **107**(2), pp. 507–513.

[12] Speziale, C., Sisto, F., and Jonnavithula, S., 1986. "Vortex simulation of propagating stall in a linear cascade of airfoils". Journal of Turbomachinery, **108**, pp. 304–312.

[13] Saxer-Felici, H., Saxer, A., Inderbitzin, A., and Gyarmathy, G., 1999. "Prediction and measurement of rotating stall cells in an axial compressor". Journal of Turbomachinery, **121**, pp. 365–375.

[14] Gao, C., Gu, C., Wang, T., and Yang, B., 2007. "Analysis of geometries' effects on rotating stall in vaneless diffuser with wavelet neural networks". International Journal of Rotating Machinery, **2007**.

[15] Lewis, R., 2004. "Study of blade to blade flows and circumferential stall propagation in radial diffusers and radial fans by vortex cloud analysis". Journal of Computational and Applied Mechanics, **5**(2), pp. 323–335.

[16] Day, I., 1993. "Active suppression of rotating stall and surge in axial compressors". Journal of Turbomachinery, **115**(1), pp. 40–47.

[17] Choi, M., Vahdati, M., and Imregun, M., 2010. "Effects of fan speed on rotating stall inception and recovery". In Proceedings of the ASME 2010 Turbo Expo, pp. 2593–2603.

[18] Day, I., 1993. "Stall inception in axial flow compressors". Journal of Turbomachinery, **115**(1), pp. 1–9.

[19] McDougall, N., Cumpsty, N., and Hynes, T., 1990. "Stall inception in axial compressors". Journal of Turbomachinery, **112**(1), pp. 116–123.

[20] Sane, S., Sekhar, D., Patil, N., and Tagade, P., 2003. "Experimental investigation of rotating stall inception in axial flow fans". In Proceedings of the International Gas Turbine Congress, GTSJ.

[21] ANSI/AMCA 210-99 ANSI/ASHRAE 51-1999, 1999. Laboratory Methods of Testing Fans for Aerodynamic Performance Rating.

[22] Hunter, A., Scarton, H., Wilt, K., Salamah, S., and Story, D., 2010. "Generator fan test facility to quantify axial flow fan aerodynamic performance". In Proceedings of the ASME 2010 Power Conference, pp. 213–217.